Journal of Energy Chemistry 92 (2024) 404–413

Contents lists available at ScienceDirect

Journal of Energy Chemistry

journal homepage: www.elsevier.com/locate/jechem

http://www.journals.elsevier.com/journal-of-energy-chemistry/

Rational design of carbon skeleton interfaces for highly reversible sodium metal battery anodes

Fenqiang Luo [a], Taiyu Lyu [a], Jie Liu [c], Peiwan Guo [a], Junkai Chen [a], Xiaoshan Feng [b,*], Dechao Wang [a,*], Zhifeng Zheng [a,*]

[a] Key Laboratory of Advanced Energy Storage Technology, Fujian Province University, Fujian Provincial Industry Technologies Development Base for New Energy, Collaborative Innovation Platform for Advanced Electrochemical Energy Storage Technology, National User-Side Energy Storage Innovation Research and Development Center, Tan Kah Kee Innovation Laboratory (IKKEM), College of Energy, Xiamen University, Xiamen 361102, Fujian, China
[b] College of Environmental Science and Engineering, Fujian Normal University, Fuzhou 350007, Fujian, China
[c] Department of Chemical Engineering, Tsinghua University, Beijing 100084, China

ARTICLE INFO

Article history:
Received 8 November 2023
Revised 9 December 2023
Accepted 10 December 2023
Available online 18 December 2023

Keywords:
Carbon skeleton
Graphited structure
Deposition mechanism
Sodium metal batteries

ABSTRACT

Sodium metal batteries (SMBs) have attracted increasing attention over time due to their abundance of sodium resources and low cost. However, the widespread application of SMBs as a viable technology remains a great challenge, such as uneven metallic deposition and dendrite formation during cycling. Carbon skeletons as sodiophilic hosts can alleviate the dendrite formation during the plating/stripping. For the carbon skeleton, how to rationalize the design sodiophilic interfaces between the sodium metal and carbon species remains key to developing desirable Na anodes. Herein, we fabricated four kinds of structural features for carbon skeletons using conventional calcination and flash Joule heating. The roles of conductivity, defects, oxygen content, and the distribution of graphite for the deposition of metallic sodium were discussed in detail. Based on interface engineering, the J1600 electrode, which has abundant Na-C species on its surface, showed the highest sodiophilic. There are uniform and rich F-Na species distributed in the inner solid electrolyte interface layer. This study investigated the different Na-deposition behavior in carbon hosts with distinct graphitic arrangements to pave the way for designing and optimizing advanced electrode materials.

© 2023 Science Press and Dalian Institute of Chemical Physics, Chinese Academy of Sciences. Published by ELSEVIER B.V. and Science Press All rights reserved.

1. Introduction

Over the last few years, lithium-ion batteries (LIBs) have dominated the global market for electrochemical energy storage [1–3]. However, LIBs become more expensive as lithium resources prove insufficient to the need for large-scale energy storage. To meet the increasing demand for advanced energy storage systems, it is crucial to explore new batteries that offer high energy density at low cost [4–6]. Amongst the potential batteries, sodium metal batteries (SMBs) stand out because of the abundant sodium resources (2.8 wt%) and high theoretical specific capacity (1165 mA h g^{-1}), low electrochemical potential (−2.71 V versus the standard hydrogen electrode) of sodium metal [7–9]. Besides, SMBs have the potential to replace LIBs due to the low cost of sodium resources, dominating the global market for renewable energy storage, electric vehicles, smart homes, etc..

However, the uneven growth of the dendrites of sodium metals during cell operation is a significant serious safety issue, which hinders its practical application [10–12]. Extensive efforts, such as alloying reactions, electrolyte modulation, construction of artificial interphases, and the utilization of solid-state electrolytes, have been used to control the formation of Na dendrites [13–17]. Additionally, incorporating Na metal into a three-dimensional (3D) structure is another effective approach that can reduce volume changes during charge and discharge cycles and minimize localized current flux [18–21]. Many different materials with a 3D structure, such as metallic or carbon-based current collectors, have been explored [22–24]. Carbon skeleton has attracted a lot of attention due to its controllable porous structure and surface properties [25,26]. Electrospinning technology is a versatile and straightforward technique among various fabrication methods for synthesizing 1D carbon nanofibers. It offers a wide range of tunable

* Corresponding authors.
E-mail addresses: fxs010066@fjpsc.edu.cn (X. Feng), wangdechao@xmu.edu.cn (D. Wang), zhifeng.zheng@xmu.edu.cn (Z. Zheng).

https://doi.org/10.1016/j.jechem.2023.12.006
2095-4956/© 2023 Science Press and Dalian Institute of Chemical Physics, Chinese Academy of Sciences. Published by ELSEVIER B.V. and Science Press All rights reserved.

macrostructures and the capability to introduce beneficial features simultaneously [27]. Polyacrylonitrile (PAN) nanofibers using dimethylformamide (DMF) as solvent is the most common route to obtain carbon skeleton due to its high carbon yields and good mechanical properties [28,29]. However, the expensive PAN resources and environmentally unfriendly DMF solution is not suitable for practical application. Lignin is an attractive alternative for PAN due to their eco-friendly nature and low cost. Lignin with highly branched structure can help generate a carbon skeleton with good mechanical properties and abundant defects, which is beneficial features for designing high reversible sodium anode [30,31].

The carbon skeleton, when modified by functional groups, can alleviate the formation of Na dendrites [32–34]. Xu et al. [35] reported that defect-rich carbon skeletons fabricated at 700 °C can regulate homogeneous sodium deposition. The carbon host with porous structures can facilitate the uniform nucleation and plating of Na metal. Although those methods alleviate corresponding problems through heteroatomic engineering and morphology design, they rarely focus on regulation of the interface for the dendrite growth, including the carbon surface and solid electrolyte interface (SEI). Some reports confirm that the F-rich SEI layer enables the protection of the underlying Na metal, revealing stable electrochemical performance. However, there is still challenge for us to optimize the SEI structure due to uneven distributed organic species and F-contenting species.

Herein, various hard carbons with distinct graphitic structures are used as 3D skeletons for SMBs. Two methods, including Joule heating and traditional heating, were used to construct different graphitized surfaces on the carbon skeleton. Compared to carbonized carbon skeletons (at 800 °C), which provides sodiophilic sites through abundant defects or function groups, the sodiated graphitized carbon skeletons (at 1600 °C) have a higher amount of sodium-carbon compounds on its surface, resulting in more induce uniform sodium deposition. The co-intercalation of solvated Na^+ into carbon skeleton is achieved by utilizing the linear ether electrolyte (diglyme). For the first time, we have discovered that the co-intercalation of hard carbon exhibits a high sodiophilic property. Na can be uniformly deposited on the fiber surface with excellent cyclic reversibility. The graphitized structure enables the formation of an F-rich SEI layer, which is more uniform than that of carbonized carbon skeleton and protects the composite anode from harmful side reactions with the electrolyte. The symmetric cells assembled with graphitized hard carbon anode display low voltage and long cycle life. The full cell with a low N/P ratio, containing a Na@J1600 anode and a $Na_3V_2(PO_4)_3$ (NVP) cathode, maintains excellent stability.

2. Experimental

Preparation of precursor film: The lignin powder (Shandong Longli Biotechnology Co.), sodium hydroxide (4.0 g), phenol, and formaldehyde with weight of 28.2, 18.8 and 58.8 g was added into a three-neck flask. Then it was heated at 82 °C for 1 h, following at 87 °C for another 2 h. Finally, the obtained solution was stirring overnight. For electrospinning, 12% polyvinyl alcohol solution was mixed with the above solution. A moderate amount of deionized water was further added to control the viscosity of the solution. A 10 mL syringe, with a feeding rate of 0.080 cm min^{-1}, was adopted to the electrospinning. The electrospinning device (ET–2525H, Ucalery Co.) provided a high pressure between a collector (Aluminum foil, −1 kV) and the needle tip (16 kV). The obtained film was finally oxidized at 150 °C and collected for the subsequent synthesis.

Flash Joule heating method: JSJ200-II (Anhui shengjia vacuum technology Co, Ltd) was used to flash Joule heating. Two graphite paper spacers were used as heater placed in two copper electrodes. The film was further stuck in the middle, contacting with the graphite paper. The devices can provide maximum voltages at ∼120 V with maximum currents of ∼220 A. For the flash Joule heating, 800/1600 °C can be achieved by using a charging voltage of 40 V and a current of 40/140 A below 0.5 Pa. The obtained carbon film was used as the electrode and marked as J800 or J1600, respectively.

Conventional calcination process: By using a tube furnace, the film was heated at 800/1600 °C for 2 h with a heating rate of 5 °C min^{-1} under an Ar atmosphere. The obtained carbon film was used as the electrode and marked as C800 or C1600, respectively.

Characterizations: The X–ray diffraction (XRD) spectra were obtained through Rigaku Ultima IV with a voltage of 30 kV and a current of 10 mA. Zeiss SIGMA and Tecnai F30 was used to observe the microstructure of the sample. The Raman spectra were obtained by using the XploRA PLUS equipped with a laser at the wavelength of 532 nm. X-ray photoelectron spectroscopy (XPS) spectra were obtained by a Thermo Scientific K-Alpha. The in-situ optical microscope was carried out by using the Nikon SMZ745 device. The electrodes after 10 cycled were used for SEI analysis, whichdisassembled and washed with diglyme, following transferred under an Ar atmosphere. The conductivity is measured by the RTS-8 four probes tester. The carbon film was cut into 3 cm × 4 cm and then transferred to the test table. The conductivity was tested three times and shown in the average value.

Electrochemical tests: The fabricated carbon film with a diameter of 9 mm (∼1.5 mg cm^{-2}) was used as electrode. The electrode was paired with Na foil and assembled into coin-type half cells (CR2032) by filling with 120 μL electrolyte (1.0 M $NaPF_6$ in diglyme) to obtained carbon/sodium electrode. The symmetrical cell was assembled with the same carbon/sodium electrode with a Na capacity of 6 mA h cm^{-2}, corresponding to ∼805 mA h g^{-1} specific capacity of the composite Na anode. The separator is glass fiber membrane. The Land CT 2001A tester was used to obtain the electrochemical performance. The full cell was used the same electrolyte and membrane as half-cell, while carbon/sodium electrode and $Na_3V_2(PO_4)_3$ were used as the anode and cathode. All the tests were carried out at ambient temperature (∼25 °C).

Calculations: Gaussian 16 software with the density functional theory (DFT) method is used to design and analysis the adsorption model. The complex models were optimized at the level of M062X-D3/6–311 + G (d, p)/SMD (Diglyme) with the static dielectric constant of 7.4. Single point energies and MOs were calculated at the M062X-D3/def2QZVPPD/SMD (Diglyme) level, and the composition of MOs was analyzed by the Mulliken method using the Multiwfn software.

3. Results and discussion

3.1. Synthesis and characterizations of various graphitized carbon fibers

The hard carbon precursor is prepared by using the electrospinning method with a lignin-based solution as described in our previous reports [36,37]. Subsequently, the hard carbon is fabricated through calcination/flash Joule heating. Typically, the conventional carbonization with a slow heating rate (5 °C s^{-1}) needs hours to finish a heating stage, while flash Joule heating with an ultrafast heating rate (∼1000 °C s^{-1}) finishes a heating process within seconds (Fig. 1a and b). By regulating the heating time and temperature, four distinct carbonized/graphitized carbon films (J800, J1600, C800, and C1600) are obtained and shown in Fig. 1(c).

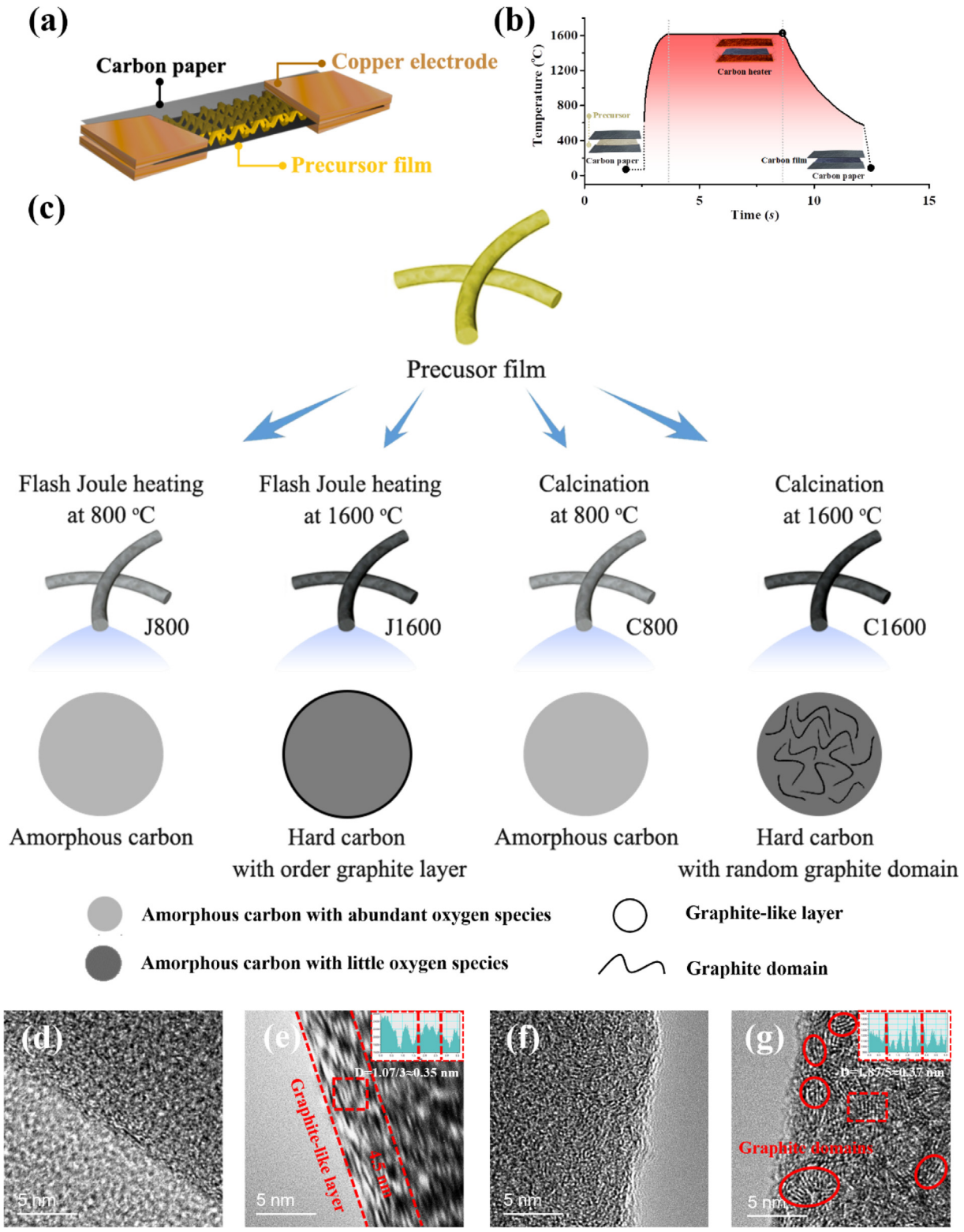

Fig. 1. (a) Schematic of the joule heating method. (b) Time-temperature curve of joule heating process. (c) Schematic synthesis of carbon host with different graphited structures by conventional carbonization and flash Joule heating. HRTEM images of (d) J800, (e) J1600, (f) C800 and (g) C1600.

After undergoing various carbonization processes, the carbon film is composed of interlaced fibers, which maintains excellent mechanical properties (Fig. S1). All the film can recover its original shape after multiple bends and folds (Fig. S2). The microstructural of the carbon film is characterized by high-resolution transmission electron microscopy (HRTEM, Fig. 1d–g and Fig. S3). As shown in Fig. 1(d and f), J800 and C800 deliver an amorphous structure without any graphite domains. In contrast, the C1600 has abundant graphite domains that are randomly distributed within the fiber, with an interlayer spacing of 3.7 nm (Fig. 1g). Notably, graphitic layers are distributed along the surface of J1600 in a long and orderly manner. The graphite layer in J1600

has a thickness of 4.5 nm and the interlayer spacing is calculated to be 3.5 nm (Fig. 1e). The more uniform the graphitic layer, the more uniform the co-intercalation. XPS characterizations of various carbonized samples further verifie the distinct graphited structures on the surface of the fibers. The surface depth of inorganic materials analyzed by XPS is near 10 nm, which only reveal the chemical state on surface area. In the high-resolution C 1*s* spectra, the sp^2-C (graphite, at ~284.0 eV) and sp^3-C (hybrid, at ~284.8 eV) can be clearly distinguished (Fig. S4) [38,39]. The J1600 shows a much stronger sp^2-C peak compared to other samples, suggesting the presence of a graphite layer. Moreover, the broad and asymmetric tail appearing at a high binding energy around 292.0 eV is evidence of a high concentration of sp^2-C in the J1600 [40]. The ratio of sp^2-C to sp^3-C is used to determine the degree of graphitization, which is calculated as 0.37, 0.50, 1.20, and 4.54 for J800, C800, C1600, and J1600, respectively. In the surface region, the J1600 delivers the highest level of graphitization. Table S1 shows that the low oxygen content of J1600 (3.5%) suggests the presence of an order graphited structure on the surface. On the other hand, the function group in J1600 cannot induce uniform sodium deposition. The high-resolution of O 1*s* spectra reveal a dominant C=O peak located at 530.8 eV and minor peaks attributed to C–O (Fig. S5). Compared with the sample heating at high temperature, J800 and C800 exhibit much higher oxygen content than those of J1600 and C1600. The abundant oxygen species in the samples can provide sodiophilic sites for sodium deposition [35].

While XPS was used to reveal the chemical state on the surface area, Raman and XRD can obtain the structural information over the whole sample. The degree of graphitization at the bulk level is characterized by X-ray diffraction (XRD) and Raman spectroscopy. Different from the highest level of graphitization observed in the XPS result for J1600, the C1600 sample exhibits the strongest and sharpest (002) peak among the four samples (Fig. S6). It means the C1600 has the highest degree of graphitization throughout the whole film. The *R*-factors, calculated based on the value of (002) peak intensity (B) and the background intensity (A), for four samples are as follows: 1.75 for J800, 1.78 for C800, 1.86 for J600 and 1.88 for C1600 (Fig. S5) [41,42]. The graphitization of the Joule heating sample is slightly lower than that of the conventional carbonization sample under the same heating temperature because the ultra-fast heating time effectively alleviated the graphitization of carbon species. The trend in Raman spectra is also consistent with XRD results (Figs. S8 and S9). The I_D/I_G ratio is 3.9, 3.0, 2.8, and 2.4 for J800, C800, J1600, and C1600, respectively.

The above results indicate that four kinds of HC are fabricated by changing the carbonization method and temperature. As shown in Table S1, the C800 is typical amorphous carbon with good conductivity. The graphitization of J800 is lower than C800, leading to poor conductivity. In contrast, the C1600 has the highest degree of graphitization, with randomly distributed abundant graphite domains. The J1600 has a unique graphitized structure with moderate graphitization at the bulk level, where the order graphite layer grows along the fiber surface.

3.2. Electrochemical analysis

The asymmetric cells (CF@Na||CF@Na) were assembled to evaluate the electrochemical performance, as CE directly measures the plating/stripping reversibility. Initially, a metal Na with a capacity of 1 mA h cm^{-2} was plated onto the host using the current density of 1 mA cm^{-2}. As shown in Fig. 2(a), the Na deposition on J1600 reveals the lowest nuclear overpotential of 21 mV. In contrast, the nuclear overpotential of Na was approximately near 30 mV for J800, C800, and C1600 electrodes. Under the current density of 1 mA cm^{-2}, the J1600 is able to provide an average CE of approximately 99.8% for 450 cycles (Fig. 2b). The J800@Na, C800@Na, and C1600@Na symmetric cells are short circuit after working for 335, 400, and 380 cycles, respectively. The voltage profiles for plating/stripping of J1600 are shown in Fig. 2(c). The host reveals a low nuclear overpotential of 21, 33, 38, 43 and 60 mV at 1, 50, 100, 200, and 400 cycles, respectively. Then, the symmetric cell is assembled by using various CF@Na electrodes, cycling at the current density of 1 mA cm^{-1} with a Na capacity of 1 mA h cm^{-1}. The Na|| Na symmetric cell was also assembled; however, it only works for less than 30 h, suggesting poor reversibility (Fig. S10). Among the four electrodes, the J800@Na symmetric cell occurred short circuits within 100 h of operation. After operating for 1000 h, a short circuit occurred in the C1600 symmetric cell. In contrast, the C800@Na and J1600@Na symmetric cell sustains reversible plating/stripping for 2000 h. The J1600@Na symmetric cell reveals a stable voltage hysteresis of 13 mV, while the C800@Na symmetric cell reveals an unstable voltage hysteresis during cycling (Fig. 2d and e). For rate performance, only the J1600@Na symmetric cell delivers a steady voltage profile under the current density of 0.5, 1, 2, 3, 4 mA cm^{-2} (Fig. 2f). The voltage profile also maintains stability when the current density returns to 0.5 mA cm^{-2}. Compared with others carbon-based/Na composite anode, the J1600/Na delivers lower voltage hysteresis and excellence cycling stability (Table S2).

Checking for inductive loops, or the absence of an imaginary loop, with impedance spectroscopy also be used to identify the presence of electronic shorts. As a control cell, the Na||C cell was assembled. As shown in Fig. S11(a), a health Na||C cell display a typical inductive loop consisting of a semicircle at high frequency region and straight line at low frequency region. In contrast, a short circuit Na||C cell does not exhibit an inductive loop in EIS test. In Fig. S11(b), the J1600-Na||J1600-Na after 10 or 100 cycles reveal a curve similar to the health Na||C, suggesting its well working situation and excellent cycling stability. The Na||Na symmetric cell also maintains health working after 10 cycles. However, the Na|| Na symmetric cell is short-circuited after more than 20 cycles and its EIS curve also reveals a useless shape.

The correlations among conductivity, graphitization, C/O ratio, C_{sp2}/C_{sp3} ratio, and Na plating/stripping behavior of SCNFs are established and shown in Fig. 2(g). Although the J800 host exhibits abundant oxygen functional groups and defects, it displays poor reversibility during the plating/stripping process due to its low conductivity (0.17 S cm^{-1}). In contrast, the C800 host, which also possesses abundant oxygen functional groups and defects, exhibits good stability due to its increased conductivity (3.26 S cm^{-1}). The amorphous, defect-rich carbon structure derived from an aromatic lignin precursor provides acceptable sodiophilicity, as previously reported [35]. Interestingly, the carbon host, fabricated at a high temperature with low defects or oxygen groups, delivers good sodiophilicity, or even superior sodiophilicity compared to C800. The J1600 host has the lowest oxygen content and the highest C_{sp2}/C_{sp3} ratio among the four samples. This indicates that the high sodiophilicity of J1600 is not primarily influenced by functional groups or defects. Based on the different voltage profiles of the electrodes mentioned above, it can be inferred that the electrochemical behaviors during the discharge process and the structures of the SEI film are crucial factors in determining sodiophilicity.

3.3. Impacts of SEI structure and carbon species

The structural evolution of the carbon host is monitored by the ex-situ XPS test (Fig. 3 and Figs. S11–S15). Prior to etching, the C 1*s* spectra of the fully discharged electrodes are divided into five primary carbon species, including C–Na, C–C, C–O, C=O, and C–F (Fig. S11) [43,44]. It is worth noting that the C–Na compound is

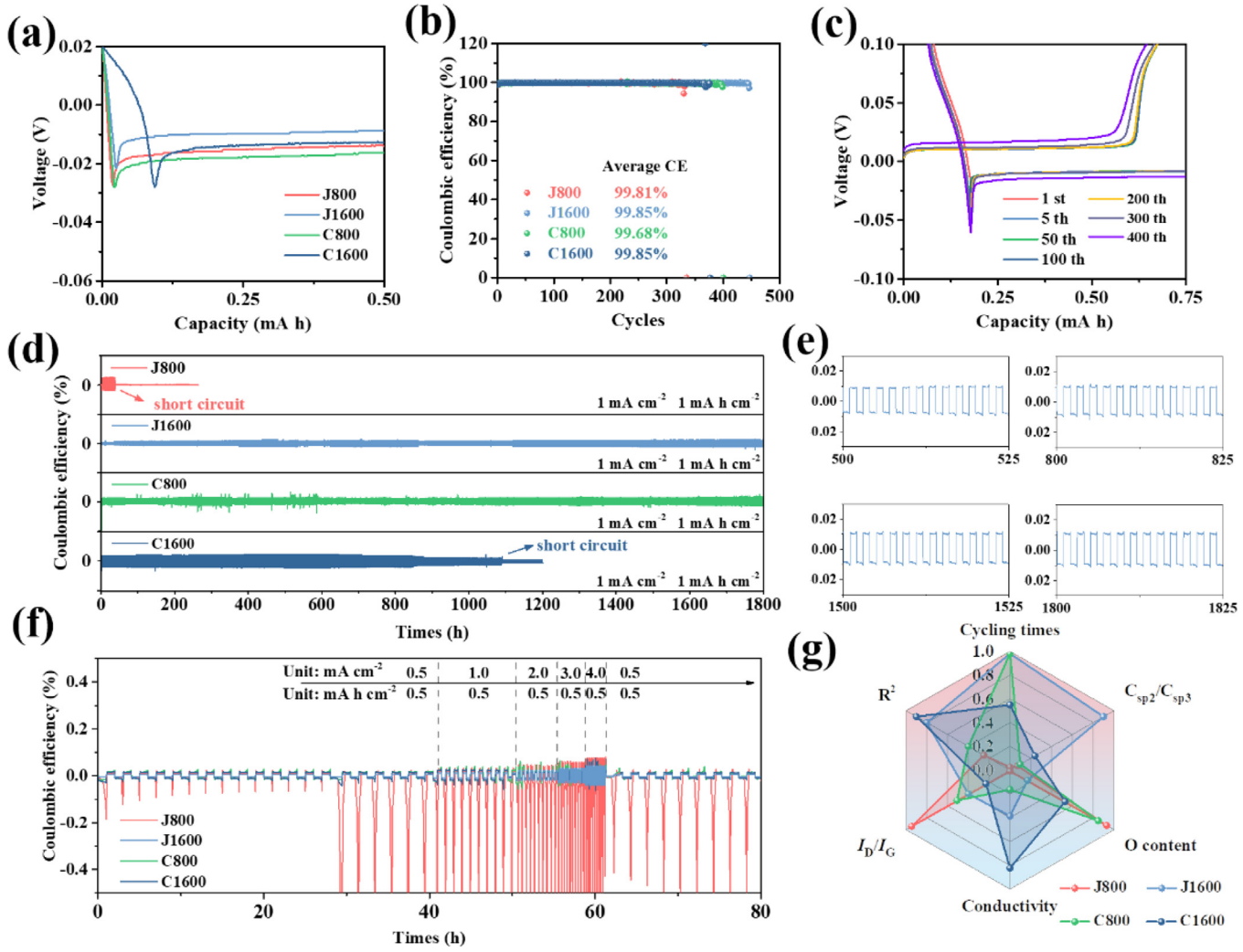

Fig. 2. (a) Voltage profiles showing the initial nucleation overpotentials of sodium deposition on J800, J1600, C800 and C1600 at 1.0 mA cm^{-2}. (b) Coulombic efficiency of sodium plating and stripping on four electrodes. (c) Voltage profiles of J1600 at different cycles. (d) Cycling stability of the symmetrical cell with various Na/C electrodes at current densities of 1 mA cm^{-2} with a specific capacity of 1 mA h cm^{-2}. (e) Enlarged plots at 500–525, 800–825, 1500–1525 and 1800–1825 h for J1600. (f) Rate performance of the symmetrical cell with various Na/C electrodes at different current densities of 0.5, 1, 2, 3, 4 mA cm^{-2}. (g) Normalized influence curve of O content, conductivity, I_D/I_G, R^2 and C_{sp2}/C_{sp3} on the stability.

exclusively observed in J1600 and C1600 (Fig. S11c and d). During the initial stages of plating, Na ions preferentially adsorb onto the graphite surface rather than crystallize into Na bulk. The low lattice mismatch between Na and graphite further induces the uniform electrodeposition. Therefore, the presence of a well-ordered quasi-graphite layer on the surface of the J1600 or the randomly distributed graphite domains in C1600 enhances their sodiophilic properties. As depicted in F 1*s* spectra, the primary species on the outermost surface for C800, C1600, and J1600 are mainly C–F, with a small F–Na component (Fig. S12) [45,46]. The J800 reveals three main peaks corresponding to C–F, F–P, and F–Na. The presence of anomalous constituents in the J800 could be attributed to the unstable decomposition of electrolytes, which is caused by poor conductive properties.

The evolution of XPS spectra with varying etching depths is shown in Fig. 3(a–h). In the figures, an upward arrow indicates an increasing trend in intensity, a downward arrow indicates a decreasing trend, and a horizontal line represents relative stability. With increasing etching depth, the signals in the C 1*s* spectra associated with many organic peaks change slightly (Fig. 3a–d). The signals in C800, C1600, and J1600 reveal a consistent trend of decreasing C–F species. The F 1*s* spectrum demonstrates a distinct gradient trend during 10 nm sputtering, shifting from a dominant C–F composition with a secondary composition of and F–Na to a dominant F–Na with a secondary composition of C–F (Fig. 3e–h). Furthermore, while the SEI layer of the pristine J1600 electrode exhibited a chemical composition and distribution of chemical species similar to that of the C1600 electrode, there is a significant difference in the varying NaF content between the two due to their distinct surface structures. Before the etching depth of 10 nm, the NaF content in the SEI layer of J1600 increased sharply to reach a peak value and then stabilized with subsequent etching (Fig. 3i–l). Extended the etching to a depth of 20 nm resulted in an almost overlapping F 1*s* spectra with those obtained at 10 nm, indicating the stable chemical composition of the SEI film (Figs. S11–S15). In contrast, the C1600 and C800 reveal an uneven distribution of organic and inorganic fluorine components within a 20 nm range. On the J1600 surface, there is more uniform F–Na species compared to others electrodes. Besides, with increasing etching depth, the rate of change in composition content tends to moderate. It is reasonable to speculate that the SEI film will achieve stability at a greater depth.

Based on the above analysis, the mechanism of Na deposition on four kinds of hosts is summarized (Fig. 3m). Although the

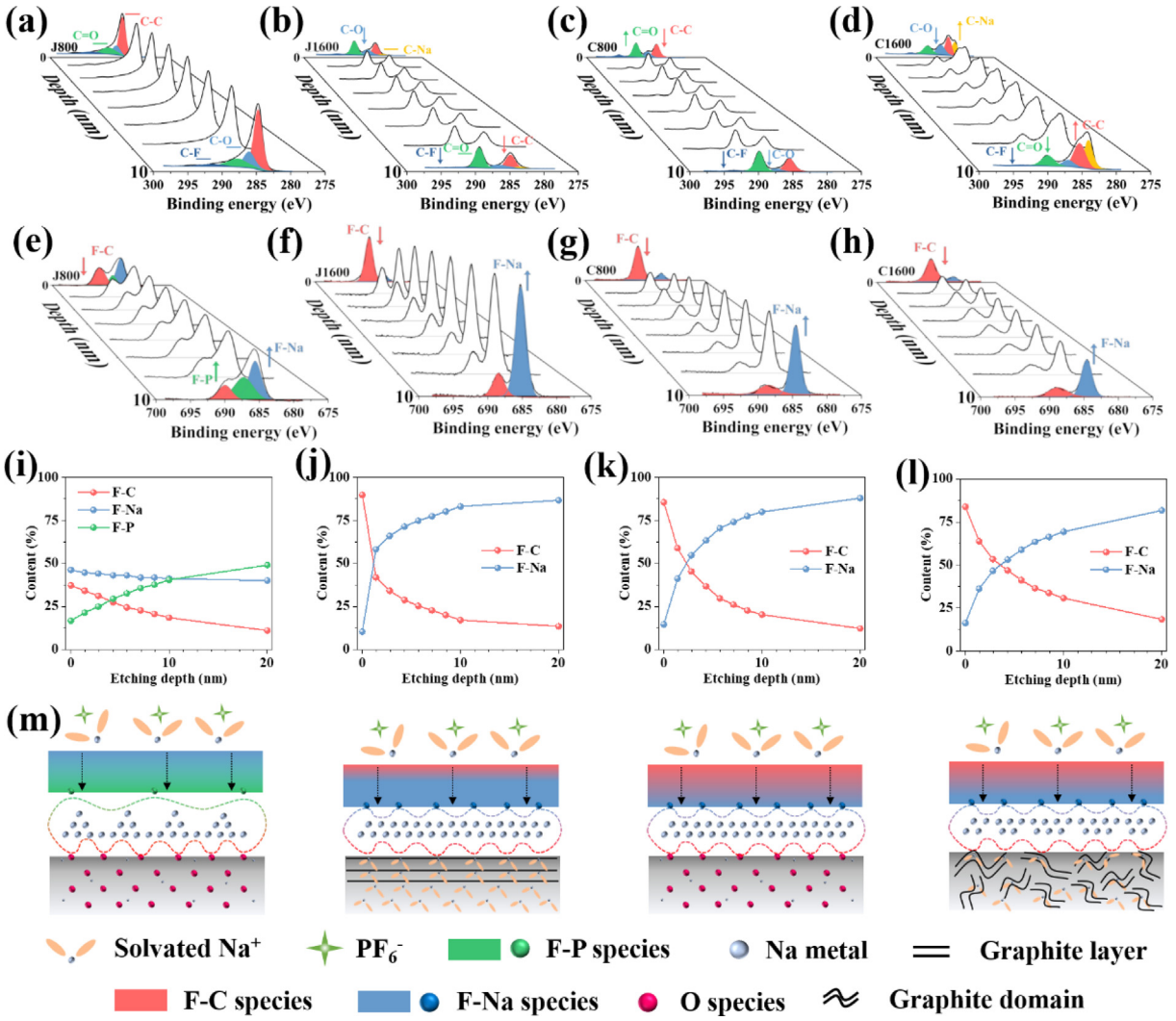

Fig. 3. The 3D waterfall graphic of (a) J800, (b) J1600, (c) C800, and (d) C1600 for C 1*s* spectra, with depth as a variable. The 3D waterfall graphic of (e) J800, (f) J1600, (g) C800, and (h) C1600 for F 1*s* spectra, with depth as a variable. The types and relative abundance of fluorine species at different depths for (i) J800, (j) J1600, (k) C800, and (l) C1600. (m) The mechanism of Na deposition on four electrodes.

J800 contains abundant oxygen functional groups, the poor conductivity of the sample leads to the formation of an SEI film lacking F-Na. These properties lead to the localized aggregation of electrons and continuous side reactions, ultimately resulting in the formation of sodium dendrites. In contrast, the SEI on C800, C1600, and J1600 have similar components. The outer layer is dominated by unevenly distributed organic species, while the inner layer becomes homogeneous and consists of abundant inorganic compounds such as NaF and Na_2CO_3. Compared to the C800 and C1600, the outer layer of the SEI on the J1600 is thinner, indicating its superior electrochemical stability. For the inner layer, NaF demonstrates exceptional Na^+ ion conductivity while remaining electronically unreactive. Due to these characteristics, the SEI layer is capable of maintaining a high transference number of Na ions and ensuring a uniform distribution of Na ions across the electrode surface. This effectively enhances the stable electrochemical performance. The C800 has abundant oxygen functional groups to effectively facilitate the uniform distribution of metallic sodium among the carbon species in the host. In contrast, the co-intercalation of C–Na species in C1600 and J1600 promotes the adsorption and electrodeposition of Na ions. Additionally, the long and uniform quasi-graphite layer on the surface of J1600 imparts better electrochemical stability compared to C1600.

The adsorption energy of C_{sp2}, C_{sp3} C_O and C_{defect} for solvated Na^+ further prove the fast adsorption behavior (Fig. S16). The solvated Na^+, that is $Na^+(Diglyme)_2PF_6^-$, is chosen as the model to be adsorbed with different carbon species. All the adsorption energy is negative, suggesting that the adsorption process can occur spontaneously. The higher adsorption energy of C_O and C_{defect} indicates that the adsorption is easier occurs on the C_O and C_{defect}. The oxygen group and defects can enhance the sodiumphilic properties of the carbon backbone by facilitating interactions with Na^+ ions. Compared with the adsorption energy of C_{sp3}, the C_{sp2} delivers higher adsorption energy, suggesting the facilitating adsorption process in C_{sp2} at the absence of oxygen and defect effects.

3.4. Sodiophilicity of carbon skeleton

To demonstrate the sodiophilicity of different carbon skeletons, two methods, including electrochemical deposition and molten sodium, are explored. As shown in Fig. 4(a), at a current density of 1 mA cm^{-1} and a minimum plating capacity of 1 mA h cm^{-1}, Na exclusively occupied the surface of the fiber. The irregularly shaped sodium dendrites are disorderedly distributed on the surface of J800, suggesting its sodiophobic property. For C1600, a number of large Na particles are observed, corresponding to the

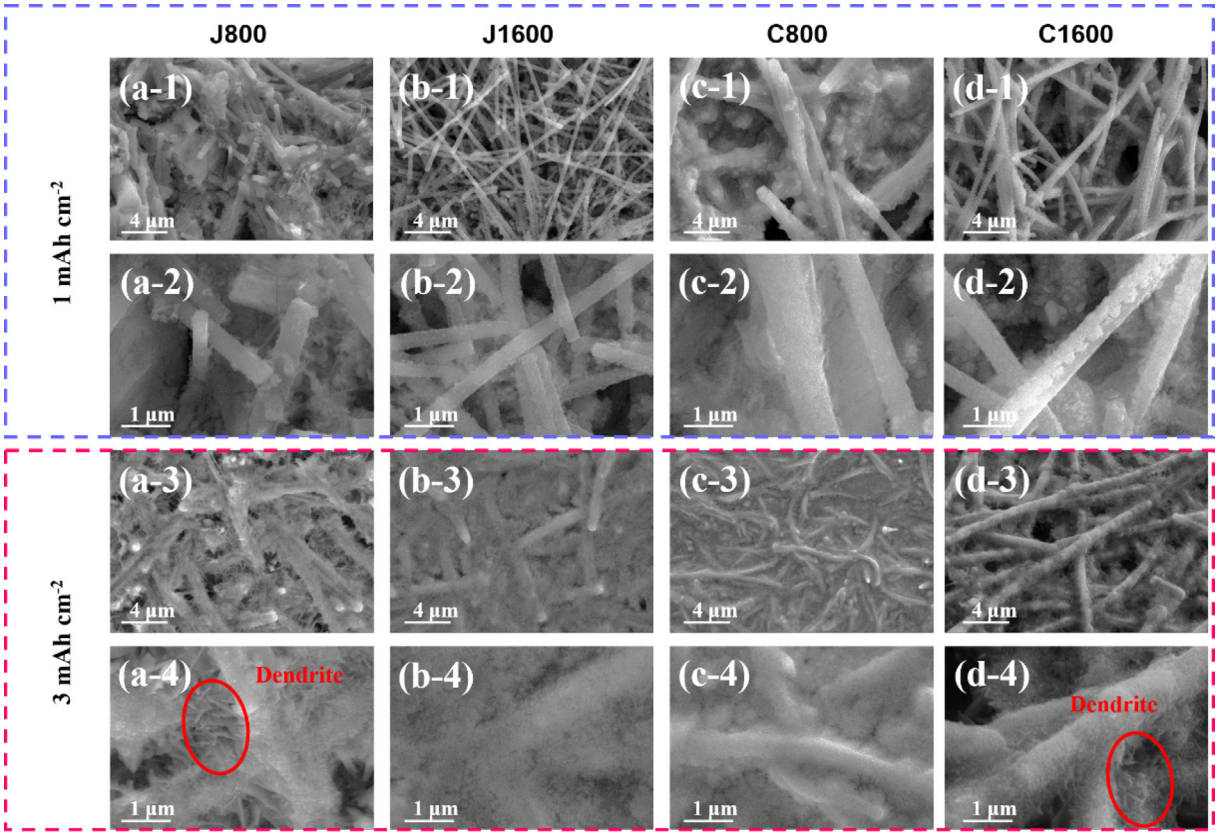

Fig. 4. SEM morphology evolution of (a) J800, (b) J1600, (c) C800, (d) C1600 electrodes filling with deposited Na capacity of (1 and 2) 1 mA h cm^{-2} and (3 and 4) 3 mA h cm^{-2}.

aggregation of metal Na. In contrast, the metal Na tends to be evenly distributed on the surface of the C800 and J1600 fibers. After increasing the deposited Na capacity to 3 mA h cm^{-2}, the deposits on J800 and C1600 hosts are filled with Na dendrites with a length of range from 0.5–2 μm. The C800 and J1600 exhibit excellent electrodeposition behavior, as continuous and small sodium particles are densely coated with fibers on their surfaces. The thickness of J800, J1600, C800 and C1600 are near 60 μm (Fig. S17). Fig. S18 shows the SEM images of four carbon skeleton after different stripping/plating cycles. Among stripping electrode after 1 cycle, the J1600 and C800 electrodes maintain clean surface, suggesting that the sodium metal is highly reversible during the plating/stripping process (Fig. S18b1, b2 and Sc1, c2). There produce a large number of dead Na on the surface of J800 only after 1 cycle, indicating the poor sodiophilicity of J800 sample (Fig. S18a1 and a2). SEM images of the plating electrode after 20 cycles also prove the high sodiophilicity of J1600 and C8000. The J1600 and C800 show uniform morphology after 20 cycles, corresponding to their high sodiophilicity (Fig. S18b3, b4 and Sc3, c4). By comparison, the poor sodiophilicity of J800 leads to the production of irregularly particle and dendrite (Fig. S18a3 and a4). Further stripped the sodium metal from the electrode, the J1600 can also maintains initial morphology (Fig. S18b5 and b6). It means the production of dead Na is alleviated so that the skeleton can maintains high sodiophilic. By comparison, dead Na is found on the surface of other samples. Enormous dead is found on the surface of J800 and C1600 (Fig. S18a5, a6 and Sd5, d6). The accumulating dead Na will gradually cover on the sodiophilic sites and finally leads to the skeleton out of action. The SEM images of the Na containing electrode after cycling also proves smooth Na deposition. As shown in Fig. S19, the metal sodium on C800 and J1600 electrode maintains its initial microstructure after 200 h cycling under the current density of 1 mA h cm^{-2}, suggesting the excellent reversibility of sodium metal.

The in-situ light microscope directly observes the deposition of Na metal on the electrode. The Na||Na asymmetric cell, with a bare Na foil, is assembled, and the cell operates under the current density of 1 mA cm^{-2} (Fig. 5a–d). During a deposition process with a duration of 20 min, a number of dendrites are observed on the surface of the Na foil. As the deposition time increases, the dendrites continued to grow, eventually leading to a short circuit after approximately 60 min. In contract, the Na@J1600||Na@J1600 asymmetric cell operates stably for 180 min, as shown in Fig. 5 (e–h). The uniform Na layer is grown on the electrode, which convincingly demonstrates the high sodiophilicity of the carbon film.

The photograph of different carbon skeleton placed on the molten sodium also demonstrates the excellent sodiophilicity of C800 and J1600. By placing the C800 onto the molten sodium metal, sodium metal readily infuses into the C800 within 30 s due to the presence of abundant defects and oxygen-containing functional group (Fig. S20a). The J1600 skeleton also enables a diffusion process of molten sodium metal within 30 s, suggesting its good sodiophilicity (Fig. S20d). The climbing of sodium metal onto the C1600 is slower than that of C800 and J1600, which takes approximately 90 s to climb onto the whole skeleton (Fig. S20c). In comparison, the J800 skeleton delivers the worst sodiophilicity among four skeletons, as the molten sodium metal is hardly to climb onto the J800 skeleton even after 90 s (Fig. S20b). This sodiophilicity of four carbon skeletons can well correspond to the electrochemical performance of the symmetrical cell.

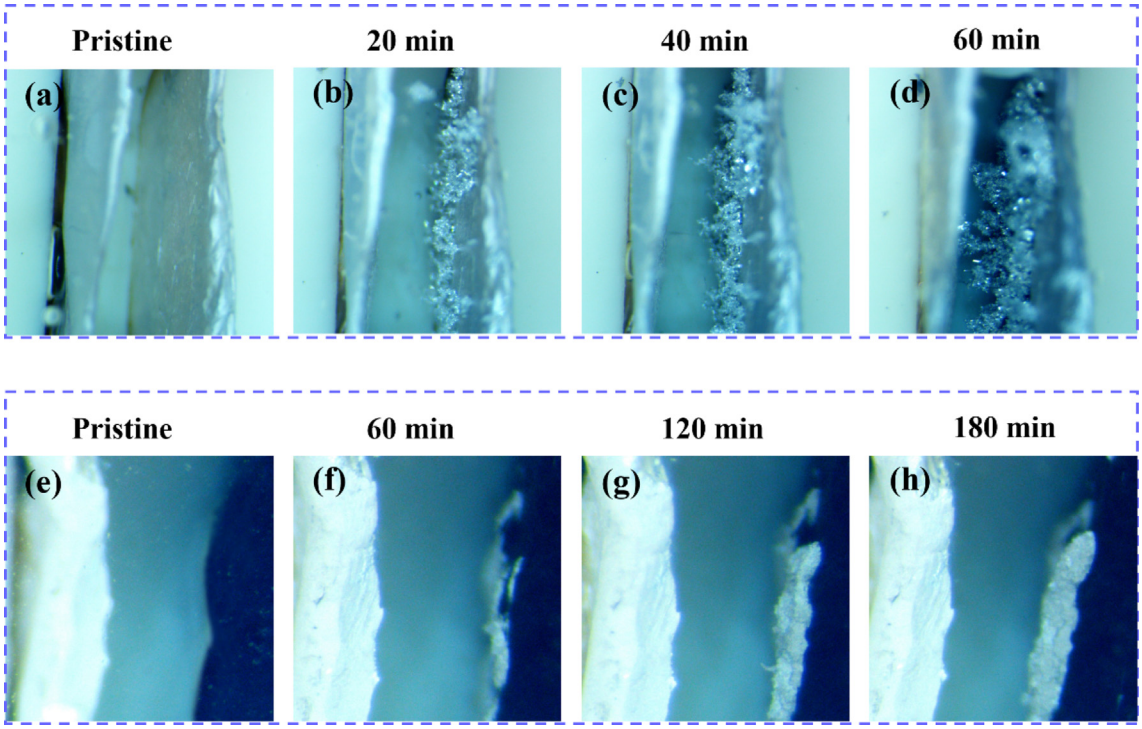

Fig. 5. In-situ light microscope of the morphology evolution of Na foil deposited after (a) 0, (b) 20, (c) 40 and (d) 60 min under the current density of 1 mA cm^{-2}. In–situ light microscope of the morphology evolution of J1600 electrode deposited after (e) 0, (f) 60, (g) 120 and (h) 180 min under the current density of 1 mA cm^{-2}.

3.5. Full cell performance

To confirm the practical application of the Na@J1600 anode, we assembled a Na@J1600||NVP full cell with an ultra-low N/P ratio of 1, as shown in Fig. 6(a). The rate capabilities are measured at different C-rates (1 C = 117 mA h g^{-1}) ranging from 0.2 to 10 C. The Na@J1600||NVP full cell demonstrates superior performance in terms of initial Coulombic efficiency, capacity retention, and rate recovery (Fig. 6b). It delivers a high capacity of 110 mA h g^{-1} with a high ICE of 97.5%. Even under the high current density of 10 C, the full cell maintains a high capacity of 82 mA h g^{-1}. When the current returns to 2 C, the capacity can quickly recover to 102 mA h g^{-1} (Fig. 6c). The reversibility of the electrode is confirmed by assembling the full cell with a low N/P ratio of 2 (Fig. 6d). The cell, with

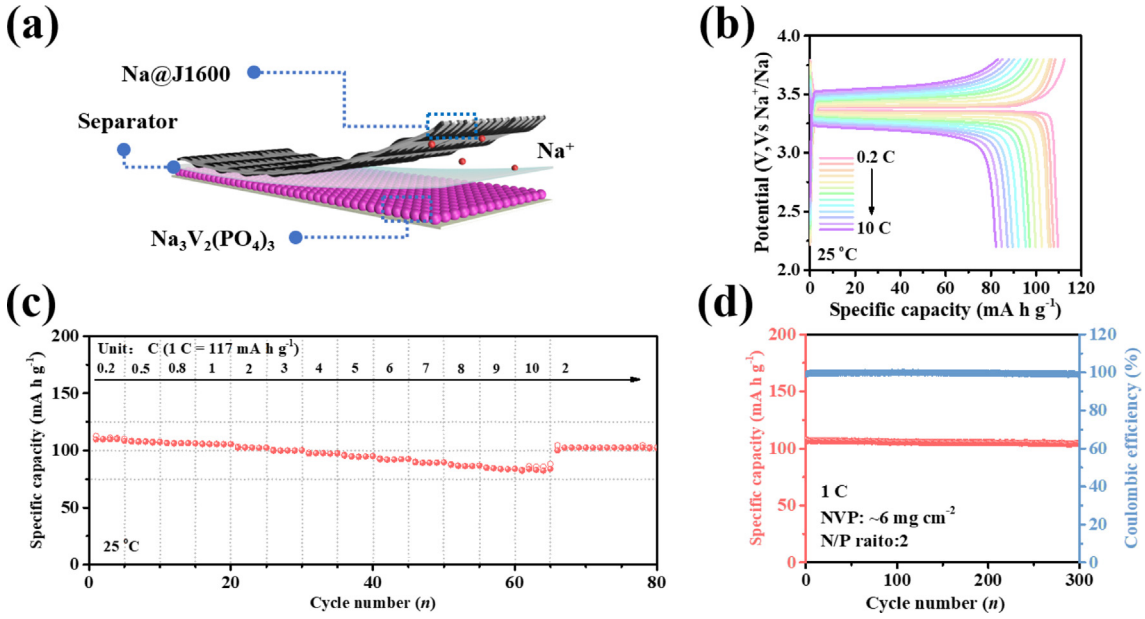

Fig. 6. (a) Schematic illustration of the Na@J1600||NVP full cell. (b) The voltage profiles of the Na@J1600||NVP full cell under different current density from 0.2–10 C. (c) Rate performance of Na@J1600||NVP full cell. (d) Cycling performance of Na@J1600||NVP full cell with high mass loading of 6 mg cm^{-1} and low N/P ratio of 2.

a cathode that has a low mass loading of 6.3 mg^{-2} (0.7 mA h cm^{-1}), delivers an excellent reversible capacity of 104 mA h g^{-1} for 300 cycles, with an average CE of 99.6 % at 1 C. The full cell studies of four carbon skeleton with low N/P raito of 1 are shown in Fig. S21. The capacity of J800@Na||NVP is fast fading at the beginning, suggesting its poor reversibility. For C1600@Na||NVP, its capacity can maintain stable before 50 cycles and gradually decreased at the following cycles. By comparison, C800@Na||NVP delivers high reversibility and has 101 mA h g^{-1} after 100 cycles. Even under the low N/P ratio of 1, the J1600@Na||NVP is able to maintain excellent stability, with a capacity retention of 78% after 200 cycles at 1 C. In comparison, the Cu@Na||NVP operates significantly unstably, exhibiting a fading capacity and oscillating CEs due to the uncontrollable side reaction and formation of inactive Na (Fig. S22). The full cell is significantly affected by anodic instability. The results prove that the carbon skeleton can alleviate the formation of Na dendrites and improve the capacity retention of SMBs.

4. Conclusions

In summary, we fabricated four types of hard carbon with different graphitized structures using either conventional carbonization or flash joule heating methods. Compared with conventional carbonization, the advantage of flash Joule heating method is reflected in the rapid synthesis and energy consumption. The J800 and C800 are both types of amorphous carbon. However, the J800 is low carbonized, resulting in low conductivity, while the C800 is fully carbonized, giving it good conductivity. The J1600 and C1600 have higher degrees of graphitization, but they differ in the distribution of graphite domains. The J1600 has a relatively orderly distributed graphite layer on the surface of the fiber and the C1600 has randomly distributed graphite domains in the whole fiber. As a result, different Na deposition behaviors occur depending on the properties of the host after being sodiated. The conductivity ensures the formation of Na-F rich SEI layer and further enhances the electrochemical stability. Notably, not only defects can enhance sodiophilic properties of carbon skeletons by promoting the interaction with Na^+ ions, but also the graphite species, especially the order graphite, benefit the uniform Na deposition. The full cell, with a low N/P ratio and high mass loading, reveals excellent reversibility for over 220 cycles, which corresponds to the energy density of 160 Wh kg^{-1}. This study provides new insights into the fundamental understanding of Na deposition in carbon hosts, specifically in terms of the graphitized structure for high-performance sodium metal anodes. Such insights are of immense significance in guiding the rational design of carbon protective layers for SMBs in the future.

Declaration of competing interest

The authors declare that they have no known competing financial interests or personal relationships that could have appeared to influence the work reported in this paper.

Acknowledgments

The work was supported by the National Natural Science Foundation of China (32271799, 31870570), the Science and Technology Plan of Fujian Provincial, China (3502ZCQXT2022001, 2020H4026, 2022G02020 and 2022H6002), and the Scientific Research Start–up Funding for Special Professor of Minjiang Scholars. The Gaussian 16 software and hardware were supported by the research group of Prof. Peifeng Su of the State Key Laboratory of Physical Chemistry of Solid Surfaces, College of Chemistry and Chemical Engineering, Xiamen University, Xiamen 361005, China.

Appendix A. Supplementary data

Supplementary data to this article can be found online at https://doi.org/10.1016/j.jechem.2023.12.006.

References

[1] M. Li, J. Lu, Z. Chen, K. Amine, Adv. Mater. 30 (2018) 1800561.
[2] J. Xie, Y.-C. Lu, Nat. Commun. 11 (2020) 2499.
[3] Y. Wang, B. Liu, Q. Li, S. Cartmell, S. Ferrara, Z.D. Deng, J. Xiao, J. Power Sources 286 (2015) 330–345.
[4] L. Hu, J. Deng, Q. Liang, J. Wu, B. Ge, Q. Liu, G. Chen, X. Yu, EcoMat 5 (2022) e12269.
[5] T. Lyu, F. Luo, D. Wang, L. Bu, L. Tao, Z. Zheng, Adv. Energy Mater. 12 (2022) 2201493.
[6] B. Wang, T. Xu, S. Huang, D. Kong, X. Li, Y. Wang, J. Mater. Chem. A 9 (2021) 6070–6088.
[7] M. Hou, Y. Zhou, F. Liang, H. Zhao, D. Ji, D. Zhang, L. Li, Y. Lei, Chem. Eng. J. 475 (2023) 146227.
[8] S. Wang, B. Peng, J. Lu, Y. Jie, X. Li, Y. Pan, Y. Han, R. Cao, D. Xu, S. Jiao, Chem. Eur. J. 29 (2022) e202202380.
[9] C. Wang, H. Wang, E. Matios, X. Hu, W. Li, Adv. Funct. Mater. 28 (2018) 1802282.
[10] M. Bai, K. Zhang, D. Du, X. Tang, Y. Liu, H. Wang, M. Zhang, S. Liu, Y. Ma, Energy Storage Mater. 42 (2021) 219–230.
[11] S.S. Chi, X.G. Qi, Y.S. Hu, L.Z. Fan, Adv. Energy Mater. 8 (2018) 1702764.
[12] B. Huang, S. Sun, J. Wan, W. Zhang, S. Liu, J. Zhang, F. Yan, Y. Liu, J. Xu, F. Cheng, Y. Xu, Y. Lin, C. Fang, J. Han, Y. Huang, Adv. Sci. 10 (2023) 2206845.
[13] T. Li, Y. Yao, Z. Huang, P. Xie, Z. Liu, M. Yang, J. Gao, K. Zeng, A.H. Brozena, G. Pastel, M. Jiao, Q. Dong, J. Dai, S. Li, H. Zong, M. Chi, J. Luo, Y. Mo, G. Wang, C. Wang, R. Shahbazian-Yassar, L. Hu, Nat. Catal. 4 (2021) 62–70.
[14] Z. Li, K. Zhu, P. Liu, L. Jiao, Adv. Energy Mater. 12 (2021) 2100359.
[15] X. Zheng, Z. Cao, Z. Gu, L. Huang, Z. Sun, T. Zhao, S. Yu, X.-L. Wu, W. Luo, Y. Huang, ACS Energy Lett. 7 (2022) 2032–2042.
[16] Y. Li, M. Li, Z. Sun, Q. Ni, H. Jin, Y. Zhao, Energy Storage Mater. 56 (2023) 582–599.
[17] Q. Jin, H. Lu, Z. Zhang, J. Xu, B. Sun, Y. Jin, K. Jiang, Adv. Sci. 9 (2022) 2103845.
[18] B. Liu, D. Lei, J. Wang, Q. Zhang, Y. Zhang, W. He, H. Zheng, B. Sa, Q. Xie, D.-L. Peng, B. Qu, Nano Res. 13 (2020) 2136–2142.
[19] N. Mubarak, F. Rehman, M. Ihsan-Ul-Haq, M. Xu, Y. Li, Y. Zhao, Z. Luo, B. Huang, J.K. Kim, Adv. Energy Mater. 12 (2022) 2103904.
[20] G. Wang, Y. Zhang, B. Guo, L. Tang, G. Xu, Y. Zhang, M. Wu, H.-K. Liu, S.-X. Dou, C. Wu, Nano Lett. 20 (2020) 4464–4471.
[21] H. Wang, Y. Wu, S. Liu, Y. Jiang, D. Shen, T. Kang, Z. Tong, D. Wu, X. Li, C.S. Lee, Small Methods 5 (2021) 2001050.
[22] Y. Xu, E. Matios, J. Luo, T. Li, X. Lu, S. Jiang, Q. Yue, W. Li, Y. Kang, Nano Lett. 21 (2020) 816–822.
[23] Y. Xu, C. Wang, E. Matios, J. Luo, X. Hu, Q. Yue, Y. Kang, W. Li, Adv. Energy Mater. 10 (2020) 2002308.
[24] L. Wang, J. Shang, Q. Huang, H. Hu, Y. Zhang, C. Xie, Y. Luo, Y. Gao, H. Wang, Z. Zheng, Adv. Mater. 33 (2021) 2102802.
[25] L. Tao, B. Ma, F. Luo, Z. Xu, Z. Zheng, H. Huang, P. Bai, F. Lin, Nano Energy 93 (2022) 106808.
[26] P. Shi, T. Li, R. Zhang, X. Shen, X.B. Cheng, R. Xu, J.Q. Huang, X.R. Chen, H. Liu, Q. Zhang, Adv. Mater. 31 (2019) 1807131.
[27] S. Li, H. Zhu, Y. Liu, Q. Wu, S. Cheng, J. Xie, Adv. Mater. 35 (2023) 2301967.
[28] F. Luo, X. Feng, L. Zeng, L. Lin, Q. Qian, Chem. Eng. J. 404 (2020) 126430.
[29] X. Li, Y. Chen, H. Huang, Y.-W. Mai, L. Zhou, Energy Storage Mater. 5 (2016) 58–92.
[30] X. Yang, Y. Zhang, M. Ye, Y. Tang, Z. Wen, X. Liu, C.C. Li, Green Chem. 25 (2023) 4154–4179.
[31] W. Fang, S. Yang, X.-L. Wang, T.-Q. Yuan, R.-C. Sun, Green Chem. 19 (2017) 1794–1827.
[32] X. Zheng, P. Li, Z. Cao, W. Luo, F. Sun, Z. Wang, B. Ding, G. Wang, Y. Huang, Small 15 (2019) 1902688.
[33] K. Yan, S. Zhao, J. Zhang, J. Safaei, X. Yu, T. Wang, S. Wang, B. Sun, G. Wang, Nano Lett. 20 (2020) 6112–6119.
[34] F. Wu, J. Zhou, R. Luo, Y. Huang, Y. Mei, M. Xie, R. Chen, Energy Storage Mater. 22 (2019) 376–383.
[35] Z. Xu, Z. Guo, R. Madhu, F. Xie, R. Chen, J. Wang, M. Tebyetekerwa, Y.-S. Hu, M.-M. Energy Environ. Sci. 14 (2021) 6381-6393.
[36] F. Luo, D. Xu, Y. Liao, M. Chen, S. Li, D. Wang, Z. Zheng, J. Energy Chem. 77 (2023) 11–18.
[37] L. Tao, A. Hu, Z. Yang, Z. Xu, C.E. Wall, A.R. Esker, Z. Zheng, F. Lin, Adv. Funct. Mater. 30 (2020) 2000585.

[38] D. Grasseschi, W.C. Silva, R.D. Souza Paiva, L.D. Starke, A.S. do Nascimento, Coordin. Chem. Rev. 422 (2020) 213469.
[39] J. Luo, J. Zhang, Z. Guo, Z. Liu, S. Dou, W.-D. Liu, Y. Chen, W. Hu, Nano Res. 16 (2022) 4240–4245.
[40] A. Kovtun, D. Jones, S. Dell'Elce, E. Treossi, A. Liscio, V. Palermo, Carbon 143 (2019) 268–275.
[41] Y. Liu, J.S. Xue, T. Zheng, J.R. Dahn, Carbon 34 (1996) 193–200.
[42] X. Yin, Z. Lu, J. Wang, X. Feng, S. Roy, X. Liu, Y. Yang, Y. Zhao, J. Zhang, Adv. Mater. 34 (2022) 2109282.
[43] Y. Chen, F. Li, Z. Guo, Z. Song, Y. Lin, W. Lin, L. Zheng, Z. Huang, Z. Hong, M.-M. Titirici, J. Power Sources 557 (2023) 232534.
[44] R. Dong, L. Zheng, Y. Bai, Q. Ni, Y. Li, F. Wu, H. Ren, C. Wu, Adv. Mater. 33 (2021) 2008810.
[45] Z. Tang, H. Wang, P.-F. Wu, S.-Y. Zhou, Y.-C. Huang, R. Zhang, D. Sun, Y.-G. Tang, H.-Y. Wang, Angew. Chem. Int. Edit. 61 (2022) e202200475.
[46] Y. Zhen, R. Sa, K. Zhou, L. Ding, Y. Chen, S. Mathur, Z. Hong, Nano Energy 74 (2020) 104895.